

Valley-symmetry-broken magnetic topological responses in $(\text{Pt}/\text{Pd})_2\text{HgSe}_3/\text{CrGeTe}_3$ and $\text{Pd}_2\text{HgSe}_3/\text{CrI}_3$ through interfacial coupling

Majeed Ur Rehman,¹ Zhenhua Qiao^{2,*} and Jian Wang^{1,†}

¹College of Physics and Optoelectronic Engineering, Shenzhen University, Shenzhen, Guangdong 518060, China

²ICQD, Hefei National Laboratory for Physical Sciences at the Microscale, CAS Key Laboratory of Strongly Coupled Quantum Matter Physics, and Department of Physics, University of Science and Technology of China, Hefei, Anhui 230026, China



(Received 8 September 2021; revised 15 March 2022; accepted 17 March 2022; published 14 April 2022)

Bringing together spin, valley, topology, and layer degrees of freedom on a single platform could establish an efficient way to engineer phenomena such as valley-symmetry-broken magnetic topological insulators. Here, we combine van der Waals (vdW) layered ferromagnetic insulators (CrGeTe_3 and CrI_3) and Kane-Mele-type topological insulators (Pt_2HgSe_3 and Pd_2HgSe_3) in the form of heterobilayers. We find that the mutual interfacial coupling turns the helical nature in $(\text{Pt}/\text{Pd})_2\text{HgSe}_3$ layers to the chiral topological nature with a large valley polarization. In particular, we identify $(\text{Pt}/\text{Pd})_2\text{HgSe}_3/\text{CrGeTe}_3$ and $\text{Pd}_2\text{HgSe}_3/\text{CrI}_3$ as quantum anomalous Hall insulators supporting a large valley polarization platform together with sizable nontrivial global band gaps ~ 32 , 17 , and 16 meV at the Fermi surface, respectively. Meanwhile, the appearance of considerable orbital magnetization in $(\text{Pt}/\text{Pd})_2\text{HgSe}_3$ layers can cause a measurable optical Kerr effect in this family of materials. Furthermore, we observe the layer-type band inversion around a single valley driven by the spin-orbit coupling in the $(\text{Pt}/\text{Pd})_2\text{HgSe}_3/\text{CrGeTe}_3$ heterobilayers, which are very rarely found in vdW layered solids. Moreover, the $(\text{Pt}/\text{Pd})_2\text{HgSe}_3$ enhances the ferromagnetic properties, such as Curie temperature of CrGeTe_3 in comparison to its freestanding form. Interestingly, the interfacial coupling of $(\text{Pt}/\text{Pd})_2\text{HgSe}_3$ drives the in-plane magnetic anisotropy energy of the freestanding CrGeTe_3 to the out-of-plane direction. In contrast, the Pt_2HgSe_3 layer switches the out-of-plane magnetic anisotropy energy of freestanding CrI_3 to the in-plane direction of the sample via an interfacial hybridization. We attribute this switching of magnetic anisotropy energy in $(\text{Pt}/\text{Pd})_2\text{HgSe}_3/\text{CrGeTe}_3$ and $\text{Pt}_2\text{HgSe}_3/\text{CrI}_3$ heterobilayers to the dominant contribution of the spin-conserving processes ($|\Delta S_z| = 0$ and $|\Delta m_z| = 0$) and ($|\Delta S_z| = 0$ and $|\Delta m_z| = 1$) in overall magnetic anisotropy energy, respectively. Our study may foster a suitable platform in which various degrees of freedom can be gathered to realize topological spintronics and valleytronics-based applications.

DOI: [10.1103/PhysRevB.105.165417](https://doi.org/10.1103/PhysRevB.105.165417)

I. INTRODUCTION

Besides the charge and spin degrees of freedom, some materials host valley degrees of freedom. When the valence band maximum and/or conduction band minimum resides on these valley points in the Brillouin zone, the valley degree of freedom becomes more relevant. For instance, graphene and its like structures such as silicene, stanene, and transition metal dichalcogenides are known examples in this context [1–4]. The valley degree of freedom adds a new subfield in the condensed matter physics referred to as valleytronics in a way similar to that in which the spin degree of freedom introduces spintronics [5,6]. Furthermore, the quantum valley Hall effect, rooted in the systems with broken inversion symmetry, has been widely explored in several valley systems [7–10]. A number of useful devices including the valley separator, valley filter, valley valve, electron beam splitter, and logic gates have been realized in valleytronics so far [11–14].

Very recently, the so-called jacutingaite (Pt_2HgSe_3) and tilkerodeite (Pd_2HgSe_3) family has been experimentally reported, which refers to the family of materials where valley physics becomes essential and warrants further exploration [15–18]. Additionally, single layers of $(\text{Pt}/\text{Pd})_2\text{HgSe}_3$ display Z_2 topological features with significant nontrivial global band gaps ~ 149 meV (at the Perdew-Burke-Ernzerhof level) due to large high spin-orbit coupling. They follow the same topological model as graphene and its like structures obey the so-called Kane-Mele model [17]. Presently, Pt_2HgSe_3 and Pd_2HgSe_3 are the only two materials that follow the Kane-Mele model with the large band splitting at the valley points.

However, the existence of valley degeneracy in the jacutingaite family limits their application, such as valley-dependent electrical transport and magneto-optical conductivity. In this context, breaking time-reversal symmetry is essential to remove the valley degeneracy at the Fermi surface of this family. Due to hosting both quantum spin Hall and valley features simultaneously, breaking time-reversal symmetry in the jacutingaite family may bring useful phenomena like valley polarization, the quantum anomalous Hall effect (QAHE), and their coexistence. This could establish a platform where both the QAHE and valley polarization can exist

*Corresponding author: qiao @ustc.edu.cn

†Corresponding author: jianwang@hku.hk

simultaneously, referred to as the valley-polarized QAHE. Among many possible routes to break the time-reversal symmetry in these systems, the best strategy is to couple them with van der Waals (vdW) ferromagnetic insulators. The vdW magnetic systems host natural cleavage surfaces free from dangling bonds and surface reconstruction issues that hinder homogeneous long-range magnetic order, and are therefore relatively easy to implement experimentally. Indeed, this approach has previously been employed for systems including graphene/CrI₃, graphene/CrGeTe₃, germanene/CrGeTe₃, CrI₃/X (X = Bi, As, Sb), and Bi₂(S/Se)₃/CrI₃ to explore the magnetic topological behavior [19–23].

In addition, to break the valley degeneracy and introduce the valley polarization, the transition metal dichalcogenides/CrI₃, stanene/CrI₃, and WS₂/VN have been discussed to explore the valley physics [24–29]. However, the Fermi level is not in the global band gap in these systems due to the considerable charge transferring at the interface, restricting the useful features such as electrical transport dominant by the valley carriers and valley-dependent optoelectronics. So far, real materials where the two phenomena, valley polarization and the QAHE, exist simultaneously are rare and need further exploration. For instance, the valley-polarized QAHE has been realized when the Co-decorated In-triangular adatom layer was epitaxially grown on Si(111) – (2 × 2) reconstructed surfaces [30]. However, the observed size of the nontrivial band gap is very small in this system, limiting its practical realization. Also, from an experimental point of view, such an approach has many complications, such as establishing long-range ferromagnetic ordering between the magnetic components of the adsorbed elements that lower the Curie temperature of the system and surface reconstruction issues due to dangling bonds on the non-vdW surfaces that cause impurity scattering hurdles. These issues can be successfully addressed by using a new strategy based on vdW layered magnetic systems with stable magnetic surfaces, where the surfaces are free from the dangling bonds and surface reconstruction issues. Very recently, new developments based on the Pt₂HgSe₃/CrI₃ system were also reported to host the valley-polarized QAHE with a moderate global band gap at the Fermi surface and high valley polarization [31]. It shows that the jacutingaite family has enormous potential both in the context of Chern insulators and valley polarization.

In order to bring the spin, valley, topology, and layer degrees of freedom on a single platform to realize the phenomena like QAHE with sizable valley polarization, we interfacially couple the vdW two-dimensional ferromagnetic systems (CrGeTe₃ or CrI₃) with (Pt/Pd)-based Kane-Mele-type topological insulators (Pt₂HgSe₃ and Pd₂HgSe₃) using the framework of heterobilayers. In this way, we break the time-reversal and spatial inversion symmetries in (Pt/Pd)-based jacutingaite family to explore the possible outcomes in the domain of valley and QAHE and their potential interplay. Furthermore, by shifting the thinking quadrant, we also study the modification in magnetic properties of CrGeTe₃ and CrI₃ layers, such as switching of magnetic anisotropy energy from in-plane to out-of-plane or vice versa and Curie temperatures due to the interfacial interaction with the Kane-Mele

topological layers. For controlling the size of nontrivial band gaps and band curvatures in the vicinity of valleys K and K' , an electric field aligned parallel or antiparallel to the sample magnetization is also considered.

We find that the interfacial hybridization with CrGeTe₃ or CrI₃ turns (Pt/Pd)₂HgSe₃ layers to be magnetic topological insulators with dissimilar Berry curvature stemming from the opposite valleys. The interplay between the magnetic proximity effects and spin-orbit coupling induces valley polarization and layer-type band inversion, enhances Curie temperature, and switches magnetic anisotropy energy from in-plane ($\parallel ab$) to out-of-plane ($\parallel c$) (or vice versa) in the proposed systems. Moreover, by adding an electric field, a phenomenon like flat bands in the vicinity of valleys K and K' can be induced, which strongly depends on the relative orientation between the applied electric field and the magnetization vector of the CrGeTe₃ or CrI₃ (i.e., parallel or antiparallel).

II. CALCULATION METHODS

In the present work, the first-principles calculations were carried out by using the pseudopotential approach under the framework of the projected augmented-wave method as implemented in the Vienna *Ab initio* Simulation Package (VASP) [32,33]. The generalized gradient approximation under the Perdew-Burke-Ernzerhof scheme was used to describe exchange-correlation interaction [34]. The cutoff energy for the plane-wave basis expansion was set to be 500 eV. In the atomic structural relaxation, all the internal degrees of freedom were allowed to relax with the tolerance parameter for force on each atom being set to be -0.01 eV/Å. For integration over the k space, a dense k -mesh grid of $11 \times 11 \times 1$ centered around the Γ point was employed. To address the strong correlation effect that is important in the case of $3d$ magnetic elements, we used the GGA + U method with the Hubbard parameter $U = 1.5$ eV and exchange energy parameter $J = 0.87$ eV [35] for the Cr $3d$ electrons. To cover vdW interaction between adjacent layers, we included the DFT-D3 method of Grimme *et al.* [36]. For the two-dimensional sheets, a slab model was used with vacuum thickness around 20 Å. The topological properties such as Berry curvatures, anomalous Hall conductivity, and Chern numbers were calculated by using the maximally localized Wannier basis as implemented in the Wannier90 and Wanniertool packages [37–39].

III. INTERFACIAL CHARACTERISTICS

In order to break the time-reversal symmetry and establish magnetic order in Pt₂HgSe₃ and Pd₂HgSe₃ layers, we interfaced them with the vdW ferromagnetic layers (e.g., CrGeTe₃ or CrI₃) having stable homogeneous magnetic ordering due to natural cleavage and stable surfaces. The interfacial adaptation of (Pt/Pd)₂HgSe₃ with CrGeTe₃ or CrI₃ layers can be analyzed by observing the parameters such as interlayer separation, charge transferring, electrostatic potential drop, and built-in electric field across the interface. Our estimated equilibrium interlayer separations are $\sim 2.51/2.50$ and 2.67 Å for the (Pt/Pd)₂HgSe₃/CrGeTe₃ and Pd₂HgSe₃/CrI₃ heterobilayers, respectively [40]. This indicates a moderate-type interfacial coupling in these heterobilayers. The interfacial

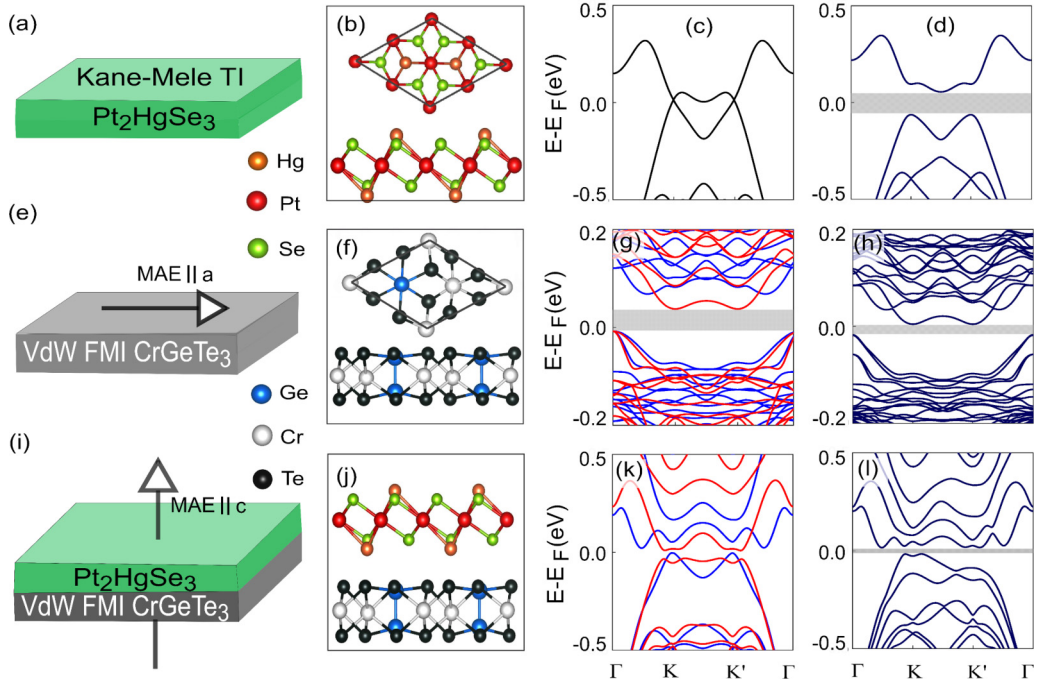


FIG. 1. (a) Schematic representation of the Kane-Mele type topological insulator Pt_2HgSe_3 in freestanding form. (b) The atomic structure of the Pt_2HgSe_3 in top and side view. (c), (d) Electronic band structure of freestanding Pt_2HgSe_3 without (c) and with (d) spin-orbit coupling. (e) Schematic illustration of the vdW ferromagnetic insulators CrGeTe_3 in freestanding form, where the horizontal arrow represents the direction of the in-plane ($\parallel a$) magnetic anisotropy energy. (f) The atomic structure of the CrGeTe_3 in top and side view. (g), (h) Electronic band structure of freestanding CrGeTe_3 without (g) and with (h) spin-orbit coupling. (i) Schematic description of $\text{Pt}_2\text{HgSe}_3/\text{CrGeTe}_3$ heterobilayer, where the vertical arrow represents the direction of out-of-plane ($\parallel c$) magnetic anisotropy energy in the system. (j) The atomic structure of the $\text{Pt}_2\text{HgSe}_3/\text{CrGeTe}_3$ in side view. (k), (l) Electronic band structure of the $\text{Pt}_2\text{HgSe}_3/\text{CrGeTe}_3$ without (k) and with (l) spin-orbit coupling. The blue and red curves correspond to the spin-up and spin-down characters, respectively.

coupling is stronger in $(\text{Pt}/\text{Pd})_2\text{HgSe}_3/\text{CrGeTe}_3$ than that in $\text{Pd}_2\text{HgSe}_3/\text{CrI}_3$. Through Bader charge analysis, we found that the charge is moved from the CrGeTe_3 or CrI_3 to $(\text{Pt}/\text{Pd})_2\text{HgSe}_3$ layer. The amount of charge transfer ΔQ is around 0.12, 0.16, and 0.005 e for the $\text{Pt}_2\text{HgSe}_3/\text{CrGeTe}_3$, $\text{Pd}_2\text{HgSe}_3/\text{CrGeTe}_3$, and $\text{Pd}_2\text{HgSe}_3/\text{CrI}_3$ systems, respectively [40]. The charge density difference plot reveals that a significant charge redistribution occurs near the interface, which establishes a potential drop across the interface, as can be seen from Fig. S1 [40]. The potential curves show that the potential drop is around 6.4, 7.86, and 5.62 eV for the $\text{Pt}_2\text{HgSe}_3/\text{CrGeTe}_3$, $\text{Pd}_2\text{HgSe}_3/\text{CrGeTe}_3$, and $\text{Pd}_2\text{HgSe}_3/\text{CrI}_3$ systems, respectively (see Fig. S1 [40]). These large potential drops establish an internal local electric field across the interface, which can lead to a spatial separation of electrons and holes in the vertical direction.

IV. ELECTRONIC PROPERTIES

When there is no spin-orbit coupling effect, Pt_2HgSe_3 and Pd_2HgSe_3 layers show a massless Dirac-type spectrum in the freestanding form where the conduction and valence bands meet at the valley points K and K' , indicating a graphene-like behavior around the Fermi surface [see Fig. 1(c) and Fig. 2(b)]. The band structure being projected over the states of different elements shows dominated contribution of the Hg- s and (Pt/Pd)- d orbitals around the Fermi level. This suggests that spin-orbit coupling may introduce large effects in

the band structures of freestanding Pt_2HgSe_3 and Pd_2HgSe_3 layers, because Hg and Pt/Pd are heavy metals exhibiting large spin-orbit coupling effects. Thus, similarly to graphene, the band gap around the K and K' is opened up when the spin-orbit coupling effects are included in these systems [see Fig. 1(d) and Fig. 2(c)]. The nature of the spin-orbit coupling is also of the so-called Kane-Mele type, as observed in graphene. However, in contrast to graphene, the size of the nontrivial band gap is larger in the Pt_2HgSe_3 or Pd_2HgSe_3 layer due to the large spin-orbit coupling in these materials.

After the deposition of $(\text{Pt}/\text{Pd})_2\text{HgSe}_3$ layers over the CrGeTe_3 or CrI_3 system, considerable magnetic exchange effects are induced in the $(\text{Pt}/\text{Pd})_2\text{HgSe}_3$ layers via proximity effects, as can be seen from Fig. 1(k) and Figs. 2(e) and 2(h). We can perceive from the band dispersion as shown in Fig. 1(k) that $\text{Pt}_2\text{HgSe}_3/\text{CrGeTe}_3$ displays electronic features similar to those of semiconductors (~ 13.0 meV at K and K' point). Around the Fermi surface, in the vicinity of the valleys K and K' , the lowermost conduction band and topmost valence band display spin-up and spin-down character, respectively. As can be observed from the layered resolved band structure as shown in Fig. 3, the dominant contribution in the vicinity of valleys K and K' mainly arises from the Pt_2HgSe_3 layer. Away from the valleys K and K' , especially in the conduction bands, the dominant contribution originates from the CrGeTe_3 layer while the valence bands overall are dominated by the states of the Pt_2HgSe_3 layer. Energy bands around the Fermi level in the $\text{Pt}_2\text{HgSe}_3/\text{CrGeTe}_3$ system are

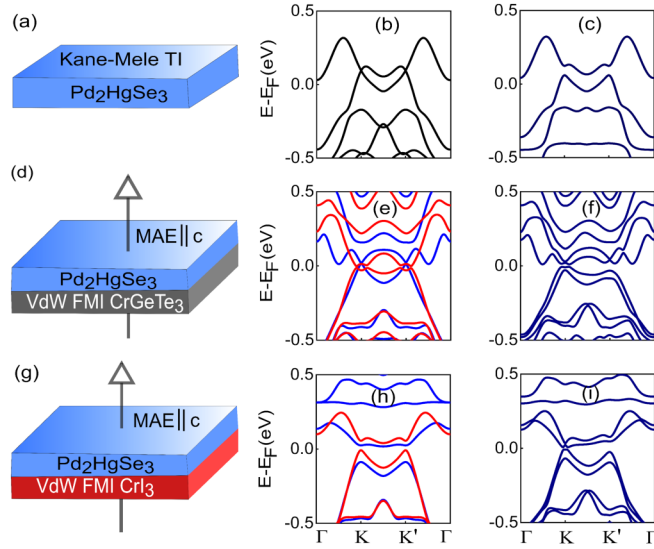


FIG. 2. (a) Schematic representation of the Kane-Mele-type topological insulator Pd_2HgSe_3 in freestanding form. (b), (c) Electronic band structure of freestanding Pd_2HgSe_3 without (b) and with (c) spin-orbit coupling. (d) Schematic description of the $\text{Pd}_2\text{HgSe}_3/\text{CrGeTe}_3$ heterostructure, where the vertical arrow symbolizes the direction of magnetic anisotropy energy in the system. (e), (f) Electronic band structure of $\text{Pd}_2\text{HgSe}_3/\text{CrGeTe}_3$ without (e) and with (f) spin-orbit coupling. (g) Schematic representation of the $\text{Pd}_2\text{HgSe}_3/\text{CrI}_3$ heterostructure, where the vertical arrow designates the direction of out-of-plane ($\parallel c$) magnetic anisotropy energy in the system. (h), (i) Electronic band structure of $\text{Pd}_2\text{HgSe}_3/\text{CrI}_3$ without (h) and with (i) spin-orbit coupling. The blue and red curves correspond to the spin-up and spin-down characters, respectively.

mostly from the Pt_2HgSe_3 layer [see Fig. 3(b)], indicating that band structure might be highly modified after the inclusion of spin-orbit coupling effects, because the Pt_2HgSe_3 layer has strong spin-orbit interaction. We found a trend similar to that expected: the band structures are highly modified. It can be seen from Fig. 1(l) and Figs. 2(f) and 2(i) that nontrivial global band gaps of different sizes are observed in $(\text{Pt}/\text{Pd})_2\text{HgSe}_3/\text{CrGeTe}_3$ and $\text{Pd}_2\text{HgSe}_3/\text{CrI}_3$ systems (see Table I).

V. VALLEY POLARIZATION AND LAYER-TYPE BAND INVERSION

Interestingly, the existing degeneracy between the opposite valleys K and K' [i.e., $E(K) = E(K')$] is also broken after the inclusion of spin-orbit coupling effect [see Fig. 1(l) and

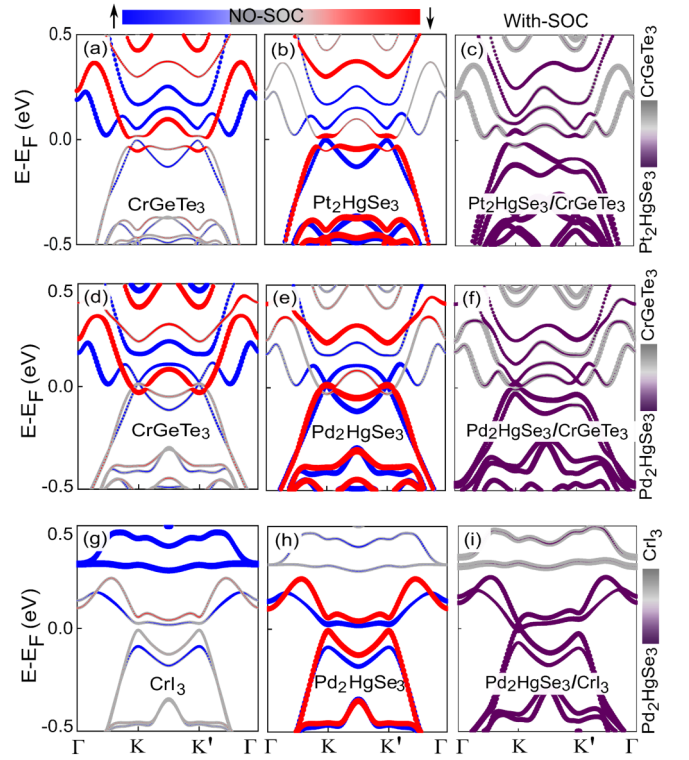


FIG. 3. (a), (b) The layer-resolved spin-polarized band structures (without spin-orbit coupling effects) of $\text{Pt}_2\text{HgSe}_3/\text{CrGeTe}_3$ heterobilayer, where the contributions coming from the spin-up and spin-down states of CrGeTe_3 (a) and Pt_2HgSe_3 (b) layers are highlighted. (c) The layer-resolved band structure (spin-orbit coupling effects included) of $\text{Pt}_2\text{HgSe}_3/\text{CrGeTe}_3$ heterobilayer. Panels (d)–(f) and (g)–(i) correspond to the $\text{Pd}_2\text{HgSe}_3/\text{CrGeTe}_3$ and $\text{Pd}_2\text{HgSe}_3/\text{CrI}_3$ heterobilayers with each panel having the same description as that of (a)–(c), respectively.

Figs. 2(f) and 2(i)]. Here, it should be noticed that spin-orbit coupling is one of the relativistic effects that links the spin and orbital angular momentum of electrons. It is commonly added as a relativistic correction to the nonrelativistic Hamiltonian in condensed matter physics. For instance, the band gaps at valleys K and K' are ~ 74 and 113 meV, respectively, reflecting highly valley-polarized behavior in the $\text{Pt}_2\text{HgSe}_3/\text{CrGeTe}_3$ system. The observed band gaps $\Delta_K/\Delta_{K'}$ at valley K/K' , spin splitting $\delta_{vv}^K/\delta_{vv}^{K'}$ between the two topmost valence bands at valley K/K' , valley splitting $\Delta_{K-K'}$, nontrivial global energy gaps E_g , and the corresponding Chern numbers \mathcal{C} for the $(\text{Pt}/\text{Pd})_2\text{HgSe}_3/\text{CrGeTe}_3$ and $\text{Pd}_2\text{HgSe}_3/\text{CrI}_3$ systems are

TABLE I. Summary of the observed size of the band gaps $\Delta_K/\Delta_{K'}$ at valley K/K' , spin splitting $\delta_{vv}^K/\delta_{vv}^{K'}$ between the two topmost valence bands at valley K/K' , valley splitting $\Delta_{K-K'}$ [$\equiv \varepsilon_{\max}(K) - \varepsilon_{\max}(K')$] with $\varepsilon_{\max}(K/K')$ representing the highest energy in the topmost valence band at valley K/K' , nontrivial global energy gap E_g , and the corresponding Chern numbers \mathcal{C} for the $(\text{Pt}/\text{Pd})_2\text{HgSe}_3/\text{CrGeTe}_3$ and $\text{Pd}_2\text{HgSe}_3/\text{CrI}_3$ systems.

Heterobilayers	Δ_K (meV)	$\Delta_{K'}$ (meV)	δ_{vv}^K (meV)	$\delta_{vv}^{K'}$ (meV)	$\Delta_{K-K'}$ (meV)	E_g (meV)	Chern number \mathcal{C}
$\text{Pt}_2\text{HgSe}_3/\text{CrGeTe}_3$	74	113	95	63	67	32	1
$\text{Pd}_2\text{HgSe}_3/\text{CrGeTe}_3$	27	69	22.5	52	24	17	1
$\text{Pd}_2\text{HgSe}_3/\text{CrI}_3$	28.5	71	29	70	16.2	16	-1

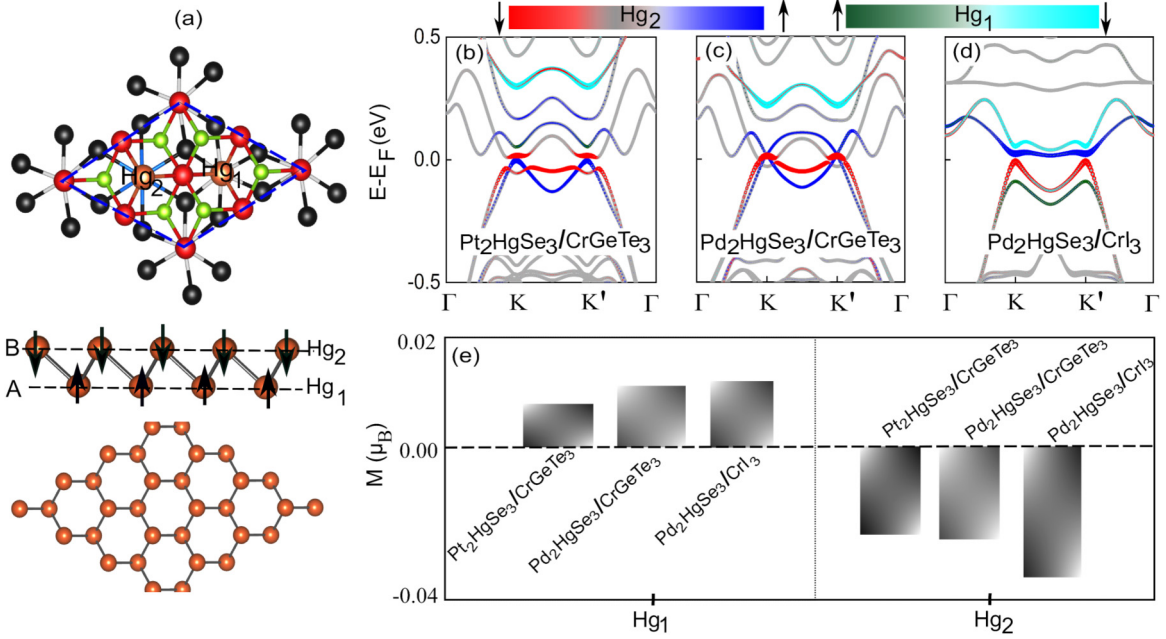


FIG. 4. (a) Top view of atomic structure configuration of the $(\text{Pt/Pd})_2\text{HgSe}_3/\text{CrGeTe}_3$ heterostructure (top) and atomic structure of the Hg atoms where the buckled-type ferrimagnetic honeycomb structure can be observed (lower). Spin-polarized band structures of the $\text{Pt}_2\text{HgSe}_3/\text{CrGeTe}_3$ (b), $\text{Pd}_2\text{HgSe}_3/\text{CrGeTe}_3$ (c), and $\text{Pd}_2\text{HgSe}_3/\text{CrI}_3$ (d), where the states are being projected over the A sublattice (i.e., Hg_1) and B sublattice (i.e., Hg_2). The dominated contribution of the B sublattice around the Fermi surface can be observed. (e) The spin magnetic moments induced on the A and B sublattices of Hg are shown for the $(\text{Pt/Pd})_2\text{HgSe}_3/\text{CrGeTe}_3$ and $\text{Pd}_2\text{HgSe}_3/\text{CrI}_3$ heterostructures where the ferrimagnetic-type magnetic behavior can be observed.

summarized in Table I. Thus, a sizable valley polarization could be achieved in the $(\text{Pt/Pd})_2\text{HgSe}_3$ layers by growing them over the ferromagnetic layers (e.g., CrGeTe_3 or CrI_3). The size of the induced valley polarization can be further controlled by external stimuli such as vertical electric field and strain effect.

More promisingly, we noticed a layered-type band inversion around valley K , where the states of Pt_2HgSe_3 and CrGeTe_3 layers become inverted as shown in Fig. 3(c). This behavior was not observed around the opposite valley K' . To our knowledge, this kind of behavior has not been reported in the vdW heterostructures so far. A similar layer-type band inversion trend was also observed in the case of Pd_2HgSe_3 over the CrGeTe_3 layer [see Fig. 3(f)]. However, the features like layer-type band inversion around the valley points were not observed in the $\text{Pd}_2\text{HgSe}_3/\text{CrI}_3$ system.

VI. ROLE OF Hg LATTICE

The role of Hg in $(\text{Pt/Pd})_2\text{HgSe}_3$ is of particular interest as it forms a buckled-type honeycomb lattice, like silicene and germanene [see Fig. 4(a)]. From Figs. 4(b)–(d), where the states are being projected over the A sublattice (i.e., Hg_1 sites) and B sublattice (i.e., Hg_2 sites), one can observe that the significant contribution in the lowermost conduction band and topmost valence band comes from the sublattice B . In contrast, the contribution of the A sublattice is away from the Fermi surface. This behavior is attributed to the inequivalent exchange field induced on the buckled Hg sites. Moreover, after coupling the $(\text{Pt/Pd})_2\text{HgSe}_3$ layers with the CrGeTe_3 or CrI_3 system, we observed that magnetic moments of different

sizes with opposite orientations are induced at the sublattices A and B as shown in Fig. 4(d). In particular, the induced spin magnetic moments M_{spn} at the Hg_1 site are parallel to the local magnetic moments of CrGeTe_3 and CrI_3 , whereas they are opposite at the Hg_2 site. This indicates that Hg atoms form a ferrimagnetic-type lattice in the $(\text{Pt/Pd})_2\text{HgSe}_3$ over the CrGeTe_3 and CrI_3 ferromagnetic layers [see Fig. 4(a)].

Figures 4(b)–(d) plot the orbital contributions of the buckled Hg honeycomb lattice in $(\text{Pt/Pd})_2\text{HgSe}_3/\text{CrGeTe}_3$ and $\text{Pd}_2\text{HgSe}_3/\text{CrI}_3$ heterostructures. Without spin-orbit coupling, the orbital contributions of the Hg_2 sites are distributed in the two bands near the Fermi energy, whereas the Hg_1 sites are separated far away from the Fermi level, which originates from the inequivalent exchange fields on the buckled Hg sites. Interestingly, we also observed a considerable size of orbital magnetization M_{orb} in the $(\text{Pt/Pd})_2\text{HgSe}_3/\text{CrGeTe}_3$ and $\text{Pd}_2\text{HgSe}_3/\text{CrI}_3$ systems [40]. For instance, our estimated orbital magnetizations are ~ 0.045 and $0.085 \mu_B$ per unit cell for $\text{Pt}_2\text{HgSe}_3/\text{CrGeTe}_3$ and $\text{Pd}_2\text{HgSe}_3/\text{CrI}_3$ systems, respectively. These orbital magnetizations are larger than the spin magnetization M_{spn} induced at the Hg sites. The appearance of the considerable orbital magnetization infers the presence of unusual phenomena like the anomalous Hall effect and Kerr effect, etc., in the jacutingaite family [41–43].

VII. REPLACEMENT OF Pt BY Pd

The appearance of Pt states around the Fermi surface suggests that electronic behavior such as the shape of the Fermi surface and band gap might be modified upon the replacement of Pt by an isovalency component such as Pd. In this

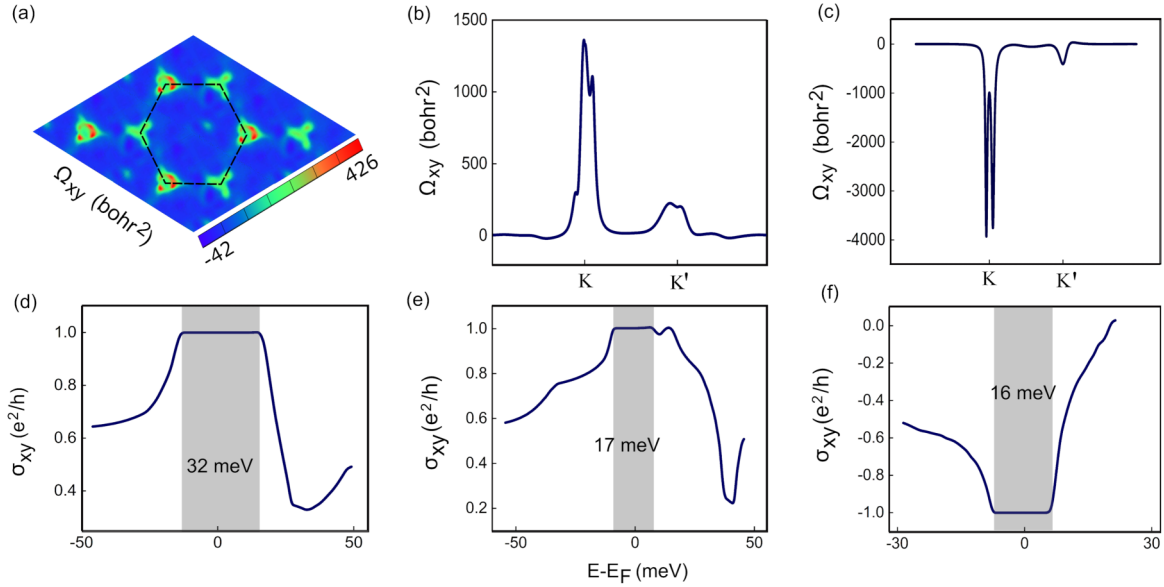


FIG. 5. Berry-curvature distribution in the first Brillouin zone along high-symmetry k points for $\text{Pt}_2\text{HgSe}_3/\text{CrGeTe}_3$ (a), $\text{Pd}_2\text{HgSe}_3/\text{CrGeTe}_3$ (b), and $\text{Pd}_2\text{HgSe}_3/\text{CrI}_3$ (c) heterobilayers, where the dominant contribution is originated from the states around valley K . The anomalous Hall conductivity versus the chemical potential for the $\text{Pt}_2\text{HgSe}_3/\text{CrGeTe}_3$ (d), $\text{Pd}_2\text{HgSe}_3/\text{CrGeTe}_3$ (e), and $\text{Pd}_2\text{HgSe}_3/\text{CrI}_3$ (f), where the plateau-type behavior in the global band gap reflects the topological hallmarks.

context, we replaced Pt with Pd in the $\text{Pt}_2\text{HgSe}_3/\text{CrGeTe}_3$ system to examine the relevant modification. In the absence of spin-orbit coupling, the $\text{Pd}_2\text{HgSe}_3/\text{CrGeTe}_3$ shows half-metallic massless Dirac-type behavior where the states in the spin-up channel form a massless Dirac-type cone at the Fermi surface, while the spin-down channel exhibits semi-conducting behavior [see Fig. 2(e)]. A similar behavior has been observed in MnX_3 ($X = \text{F}, \text{Cl}, \text{Br}, \text{I}$) systems [44]. Similarly to the $\text{Pt}_2\text{HgSe}_3/\text{CrGeTe}_3$ system, the band structure of $\text{Pd}_2\text{HgSe}_3/\text{CrGeTe}_3$ is also modified when spin-orbit coupling effects are considered. Here it should be noted that the Pt_2HgSe_3 layer shows an immense size of the nontrivial band gap in comparison to the Pd_2HgSe_3 layer when they are in freestanding form due to the large spin-orbit coupling in the Pt_2HgSe_3 layer [see Fig. 1(d) and Fig. 2(c)]. For instance, the nontrivial band gap reduces about four orders in magnitude in the case of the freestanding Pd_2HgSe_3 layer. The same trend was also observed in the Pd_2HgSe_3 layer after establishing its coupling with CrGeTe_3 and CrI_3 magnetic layers. For instance, the size of the nontrivial band gap reduces from 32 to 17 meV when we replace Pt with Pd in $\text{Pt}_2\text{HgSe}_3/\text{CrGeTe}_3$ [see Fig. 2(f)]. Similarly, the band gap reduces to 16 meV by replacing Pt with Pd in the $\text{Pt}_2\text{HgSe}_3/\text{CrI}_3$ system [see Fig. 2(i)]. The replacement of Pt by Pd also affects the size of valley polarization. For instance, the direct band gaps at K and K' are ~ 27 and 69 meV (29 and 71 meV), when Pt is replaced by Pd in $\text{Pt}_2\text{HgSe}_3/\text{CrGeTe}_3$ ($\text{Pt}_2\text{HgSe}_3/\text{CrI}_3$) systems that can be observed from Fig. 1 and Fig. 2. This trend shows that the size of valley polarization strongly depends on the type of heavy metals in the jacutingaite family.

VIII. MAGNETIC TOPOLOGICAL RESPONSE

In order to confirm the topological response of the $(\text{Pt}/\text{Pd})_2\text{HgSe}_3/\text{CrGeTe}_3$ and $\text{Pd}_2\text{HgSe}_3/\text{CrI}_3$ systems, we

estimated the topological parameters like Berry curvatures, Chern numbers, and anomalous Hall conductivity, which are commonly used to characterize the topological insulators. By using the expression

$$\Omega_{xy}(k) = - \sum_{\epsilon_{nk} \leq \mu} \sum_{m \neq n} \frac{2Im \langle u_{nk} | \hat{v}_x | u_{mk} \rangle \langle u_{mk} | \hat{v}_y | u_{nk} \rangle}{(\epsilon_{nk} - \epsilon_{mk})^2},$$

we determined the Berry curvature, where μ and $\hat{v}_{x/y}$ represent the chemical potential and the velocity operator, respectively. The distribution of the Berry curvatures over the Brillouin zone is shown in Fig. 5, where it can be seen that the Berry curvatures at valleys K and K' have different peak sizes, reflecting the valley-polarized nature in the proposed systems. Furthermore, we calculated the anomalous Hall conductivity $\sigma_H [\equiv C e^2/h]$ by using the chemical potential μ as a free varying parameter. The plateau-type behavior within the energy gap at the Fermi surface can be clearly observed from Fig. 5, reflecting the robust topological nature in these systems. The simultaneous existence of immense valley polarization with dissimilar Berry curvatures stemming from the two valleys and nonzero Chern numbers makes the $(\text{Pt}/\text{Pd})_2\text{HgSe}_3/\text{CrGeTe}_3$ and $\text{Pd}_2\text{HgSe}_3/\text{CrI}_3$ systems useful for the applications based on the coexistence of valley polarization and QAHE.

IX. FLAT-BAND APPEARANCE

The role of the Hg lattice in our proposed heterobilayers is of particular interest because it is linked to the tunability of the properties hosted by these Pt/Pd-based heterobilayers against external stimuli such as a vertical electric field. Although jacutingaite is a family of ternary materials having many differences with the Xene family (graphene, silicene, etc.), the Hg atoms in this family form a buckled-type honeycomb

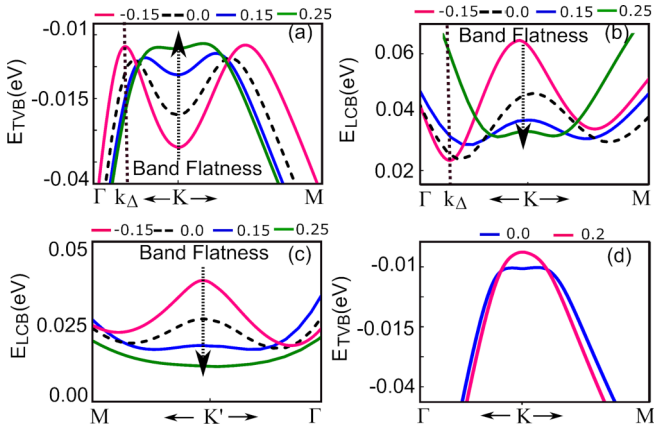


FIG. 6. Controlling the band curvature such as band flatness and location of minimum energy gap with the application of vertical electric field. (a) Topmost valence band of $\text{Pt}_2\text{HgSe}_3/\text{CrGeTe}_3$ around the valley K at different strengths of the electric field with $(E_z \uparrow \uparrow M)$ and $(E_z \downarrow \uparrow M)$ orientations. $k_\Delta [\equiv |K - k|]$ represents the finite momentum where the minimum energy gap exists in the Brillouin zone. The flat-band appearance and $k_\Delta \rightarrow 0$ can be noticed for the case $(E_z \uparrow \uparrow M)$. (b) Lowermost conduction band of $\text{Pt}_2\text{HgSe}_3/\text{CrGeTe}_3$ around the valley K at different strengths of the electric field with $(E_z \uparrow \uparrow M)$ and $(E_z \downarrow \uparrow M)$ orientations. (c) Lowermost conduction band of $\text{Pt}_2\text{HgSe}_3/\text{CrGeTe}_3$ around the valley K' at various strengths of the electric field with $(E_z \uparrow \uparrow M)$ and $(E_z \downarrow \uparrow M)$ orientations. The increase in the level of flatness of the band can be observed as we increase the strength of the electric field with $(E_z \uparrow \uparrow M)$ orientation. (d) The topmost valence band of $\text{Pd}_2\text{HgSe}_3/\text{CrI}_3$ around the valley K at different strengths of the electric field with $(E_z \uparrow \uparrow M)$ orientation. The strengths of applied electric field are shown by colored horizontal lines in the unit of $\text{V}/\text{\AA}$ (see the top of each plot).

structure like the Xene family [see Fig. 4(a)]. Also, the significant contribution in the band structures around the Fermi level [see Figs. 4(b)–4(d)] is originated from the Hg atoms. Thus due to comprising the buckled-type honeycomb geometry (like Xene solids) of the Hg lattice together with the significant contribution of the Hg atoms around the Fermi level, the bands around the Fermi level can be easily controlled by exposing the jacutingaite family to the vertical electric field. In this context, we employed the vertical electric field as an external stimulus to further tune the properties of the jacutingaite family, such as Fermi surface morphology, the size of nontrivial global band gaps, and the size of valley splittings. For instance, by exposing the $(\text{Pt}/\text{Pd})_2\text{HgSe}_3/\text{CrGeTe}_3$ system to the vertical electric field in the parallel direction of the magnetization $(E_z \uparrow \uparrow M)$, the minimum band gap which is located at some finite momentum $k_\Delta [\equiv K - k]$ can be moved exactly to the valley K , i.e., $k_\Delta \rightarrow 0$ (see Fig. 6). In other words, the level of flatness in the topmost valence band and lowermost conduction band increases as we apply the electric field in the parallel direction of the magnetization (see Fig. 6). Here, it should be mentioned that flat bands are remarkably interesting, because electrons become dispersionless in these bands (having larger effective mass), leading to a wide range of physical phenomena including high- T_c superconductivity, magnetism, and topological hallmarks [45,46]. Conversely, the region around the valleys K and K' becomes more curved

when the electric field and magnetization are antiparallel. Similarly, the spin splitting in the conduction or valence bands can be increased [decreased] by using the $(E_z \uparrow \uparrow M)$ [$(E_z \downarrow \uparrow M)$] electric field.

X. MAGNETIC ANISOTROPY SWITCHING

So far, we have focused on the possible modifications induced in the $(\text{Pt}/\text{Pd})_2\text{HgSe}_3$ system due to the magnetic layers (CrGeTe_3 and CrI_3). Now we ask the question, can the deposition of $(\text{Pt}/\text{Pd})_2\text{HgSe}_3$ modify the ferromagnetic properties like magnetic anisotropy energy and Curie temperatures of the CrGeTe_3 and CrI_3 systems? To answer this question, we performed a number of noncollinear calculations, where the spin moments are allowed to align in the out-of-plane ($\parallel c$) and in-plane ($\parallel ab$) directions. Magnetic anisotropy energy, which is referred to as the total energy difference between the out-of-plane ($\parallel c$) and in-plane ($\parallel a$) spin configurations, is considered as one of the powerful parameters for establishing long-range ferromagnetic order in low-dimensional systems. By employing the noncollinear spin-orbit coupling calculations, we first determined the magnetic anisotropy energy of the freestanding CrGeTe_3 layer. We found that the magnetic anisotropy energy of the freestanding CrGeTe_3 layer lies in the plane of the sample with an estimated size ~ -0.1 meV [see Fig. 7(a)]. This is completely consistent with previous results [47]. This in-plane magnetic anisotropy energy is unable to produce a spin-wave gap, and this is the reason that no long-range ferromagnetic ordering has been observed in the single-layer CrGeTe_3 so far. In order to understand the magnetic anisotropy energy mechanism for the ferromagnets, it is very useful to distinguish the contributions from the spin-conserving and spin-flipping processes in the overall magnetic anisotropy energy, because they are in competition in many cases and behave differently in different magnetic systems. In principle, the overall magnetic anisotropy energy is approximately equal to the sum of these two contributions (see Eq. (S5) in the Supplemental Material [40]). More specifically, $|\Delta S_z| = 0$ ($|\Delta S_z| = 1$) represents the transition between the same or parallel (opposite or antiparallel) spin states. Both the spin-conserving (i.e., $|\Delta S_z| = 0$) and spin-flipping (i.e., $|\Delta S_z| = 1$) processes can add a positive or negative contribution to the overall magnetic anisotropy energy, which depends on the value of $|\Delta m_z|$. $|\Delta m_z|$ represents the difference in the magnetic quantum number m_z of the states involved in the transition between the occupied and unoccupied angular orbital states. Whether the net magnetic anisotropy energy will lie in the plane or out of the plane of the sample or not depends on the contribution of spin-conserving and spin-flipping energies in the overall magnetic anisotropy energy. The in-plane magnetic anisotropy energy in the freestanding CrGeTe_3 is due to the dominant contribution of the spin-conserving process, which is ($|\Delta S_z| = 0$ and $|\Delta m_z| = 1$). In principle, the ($|\Delta S_z| = 0$, $|\Delta m_z| = 1$) process adds a negative contribution while the ($|\Delta S_z| = 0$, $|\Delta m_z| = 0$) process supports a positive contribution in the overall magnetic anisotropy energy (see Supplemental Material for more details [40]). Interestingly, after establishing the interfacial coupling between CrGeTe_3 and $(\text{Pt}/\text{Pd})_2\text{HgSe}_3$, the magnetic anisotropy energy switches from the in-plane to the out-of-plane direction, which can be

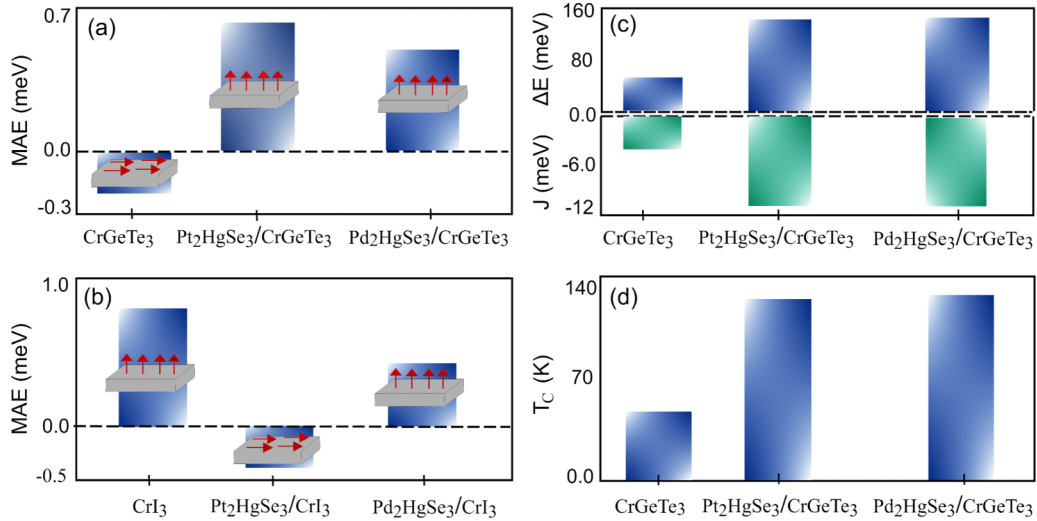


FIG. 7. Ferromagnetic properties such as magnetic exchange energies, magnetic anisotropy energy, and Curie temperatures of $(\text{Pt/Pd})_2\text{HgSe}_3/\text{CrGeTe}_3$ and $(\text{Pt/Pd})_2\text{HgSe}_3/\text{CrI}_3$ systems. (a) Magnetic anisotropy energy size of the freestanding CrGeTe_3 and $(\text{Pt/Pd})_2\text{HgSe}_3/\text{CrGeTe}_3$ heterobilayers. The switching of magnetic anisotropy energy from in-plane to out-of-plane via interfacial coupling can be noticed from the red arrows. (b) Magnetic anisotropy energy size of the freestanding CrI_3 and $(\text{Pt/Pd})_2\text{HgSe}_3/\text{CrI}_3$ heterostructure. The switching of magnetic anisotropy energy from out-of-plane to in-plane in the case of $\text{Pt}_2\text{HgSe}_3/\text{CrI}_3$ can be noticed. The horizontal dashed line in (a) and (b) represents the zero magnetic anisotropy energy (i.e., $[E(\parallel ab) - E(\parallel c)] \approx 0$), where $E(\parallel ab)$ and $E(\parallel c)$ represent the system total energy in the presence of spin-orbit coupling when all the spins are adjusted parallel in the plane and out of the plane of the sample, respectively. (c) Magnetic exchange energy and Heisenberg exchange parameters of the freestanding CrGeTe_3 and $(\text{Pt/Pd})_2\text{HgSe}_3/\text{CrGeTe}_3$ systems. (d) Curie temperatures of the freestanding CrGeTe_3 and $(\text{Pt/Pd})_2\text{HgSe}_3/\text{CrGeTe}_3$.

seen from Fig. 7(a). This out-of-plane magnetic anisotropy energy stabilizes the long-range ferromagnetic order in the CrGeTe_3 system because it can open up a spin-wave gap and thus suppress the magnetic fluctuations. We attributed this switching of magnetic anisotropy energy to the dominant contribution of the spin-conserving term ($|\Delta S_z| = 0$ and $|\Delta m_z| = 0$) in the overall magnetic anisotropy energy. Similarly, we also investigated the effects on the magnetic anisotropy energy of CrI_3 by coupling it with the $(\text{Pt/Pd})_2\text{HgSe}_3$ system. Our estimated magnetic anisotropy energy for freestanding CrI_3 is ~ 0.88 meV, which is in good agreement with the previous experimental and theoretical results [48]. We noticed that the magnetic anisotropy energy of the freestanding CrI_3 becomes lower in magnitude after interfacial interaction with the Pd_2HgSe_3 system [see Fig. 7(b)]. However, it still remains parallel to the c axis. On the other hand, the easy axis of freestanding CrI_3 shifts from the c axis to the plane of the sample, when it is grown on the surface of Pt_2HgSe_3 [see Fig. 7(b)].

The orbital-resolved spin-polarized band structure (see Fig. S5 [40]) together with Eq. (S5) [40] explains the possible origin behind the weakening of the out-of-plane magnetic anisotropy energy in $\text{Pd}_2\text{HgSe}_3/\text{CrI}_3$ and switching of magnetic anisotropy energy in $\text{Pt}_2\text{HgSe}_3/\text{CrI}_3$ from the out-of-plane ($\parallel c$) to in-plane ($\perp c$) direction. Our analysis shows that the contribution of the ($|\Delta S_z| = 0$, $|\Delta m_z| = 1$) process becomes more significant when CrI_3 is grown on the Pd_2HgSe_3 layer, which in principle reduces the size of positive magnetic anisotropy energy of freestanding CrI_3 when grown on the Pd_2HgSe_3 layer [see Fig. 7(b)]. When Pd is replaced by Pt to make the $\text{Pt}_2\text{HgSe}_3/\text{CrI}_3$ system, the contribution of the ($|\Delta S_z| = 0$, $|\Delta m_z| = 0$) process further reduces and

becomes lower in magnitude than the ($|\Delta S_z| = 0$, $|\Delta m_z| = 1$) process (see Fig. S5(b) [40]). Therefore, the overall magnetic anisotropy energy of $\text{Pt}_2\text{HgSe}_3/\text{CrI}_3$ switches from the out-of-plane to the in-plane direction [40].

XI. ENHANCEMENT OF CURIE TEMPERATURES

Together with magnetic anisotropy energy and magnetic exchange interactions, the investigation of magnetic ordering temperatures is also important. In this context, we also uncovered the effects on the magnetic exchange interaction and Curie temperatures of the CrGeTe_3 and CrI_3 by coupling them with $(\text{Pt/Pd})_2\text{HgSe}_3$ layers. By using the Heisenberg spin model and considering only the nearest-neighbor interaction, we estimated the magnetic exchange parameters J , which is around ~ -3.97 meV [40] for the freestanding CrGeTe_3 layer. Consequently, using the mean-field theory, the estimated Curie temperature of the freestanding CrGeTe_3 was found to be ~ 46 K [see Fig. 7(d)], which agrees with the experimental value ~ 35 K [47,49]. After coupling CrGeTe_3 with $(\text{Pt/Pd})_2\text{HgSe}_3$, we found a considerable enhancement in the magnetic exchange parameters and Curie temperatures that can be seen from Figs. 7(c) and 7(d). This indicates that CrGeTe_3 becomes ferromagnetically more stable after interfacing with the $(\text{Pt/Pd})_2\text{HgSe}_3$ system. For instance, the Curie temperature of the CrGeTe_3 rises to 124 K and 125 K [see Fig. 7(d)] after establishing its coupling with Pt_2HgSe_3 and Pd_2HgSe_3 , respectively [40]. Thus by coupling $(\text{Pt/Pd})_2\text{HgSe}_3$ with vdW ferromagnetic insulators such as CrGeTe_3 , issues like (i) low electronic excitation gap and (ii) low Curie temperature in QAHE can be addressed. Here it

should be noted that these are the current two major issues that restrict the application of the QAHE to a lower temperature.

XII. SUMMARY

In conclusion, by using the strategy based on the magnetic vdW layered materials, which offer a layered platform for creating a relatively clean interface to eliminate the impurity scattering and support to establish homogeneous long-range magnetization, we combined the Kane-Mele-type topological insulators (Pt/Pd)₂HgSe₃ with ferromagnetic insulators CrGeTe₃ or CrI₃. In this context, we examined the effect of interfacial coupling on the spin, valley, and topological properties, including magnetic topological hallmarks, valley polarization, magnetic exchange interaction, magnetic anisotropy energy, and Curie temperatures. Overall, we found that the interfacial hybridization of CrGeTe₃ or CrI₃ not only switches the helical nature of the (Pt/Pd)₂HgSe₃ to the chiral one but also breaks the valley degeneracy (large valley splitting) with dissimilar Berry curvatures arising from the opposite valleys. Meanwhile, the appearance of considerable orbital magnetization in the (Pt/Pd)₂HgSe₃ layers, larger than spin magnetization, can lead a phenomenon like the optical Kerr effect. We also observed the layer-type band inversion driven by spin-orbit coupling in (Pt/Pd)₂HgSe₃/CrGeTe₃, which has not been reported in the topological-based system to our knowledge so far. Thus, by interfacing the jacutingaite family with the vdW layered ferromagnetic insulators, a suitable platform could be established where the coexistence of the phenomena like valley polarization and QAHE can be regarded.

The nontrivial global band gap, size of valley splitting, and flatness of the bands around valley K and K' can be further tuned with the application of the electric field depending on the relative orientation of the electric field and magnetization. For instance, by exposing (Pt/Pd)₂HgSe₃/CrGeTe₃ to a vertical electric field, we observed two modifications in the band structure in the vicinity of valley K and K' around the

Fermi surface: (i) around the valley K and K' , the level of flatness in the topmost valence band and lowermost conduction band increases (decreases) as we apply the electric field in the parallel (antiparallel) direction of the magnetization. (ii) The minimum band gap at the finite momentum k_Δ is shifted toward valley K (away from valley K) when $E_z \uparrow \uparrow M$ ($E_z \downarrow \downarrow M$).

On the other hand, the Kane-Mele topological insulators (Pt/Pd)₂HgSe₃ strongly modify the ferromagnetic nature of the vdW layered ferromagnetic insulators CrGeTe₃ and CrI₃. For instance, the Curie temperatures of the CrGeTe₃ reach 124 and 125 K after interfacial hybridization with (Pt/Pd)₂HgSe₃. Furthermore, the in-plane magnetic anisotropy energy in freestanding CrGeTe₃ turns to be out-of-plane when it is epitaxially grown on the surface of (Pt/Pd)₂HgSe₃. In contrast, the out-of-plane magnetic anisotropy energy in CrI₃ turns out to be in the plane of the sample due to interfacial hybridization with Pt₂HgSe₃, which is attributed to the dominated contribution of the spin-conserving process ($\Delta S_z = 0$ and $|\Delta m_z| = 1$) in overall magnetic anisotropy energy. Due to forming a buckled-type honeycomb geometry of the Hg atoms together with the major contribution around the Fermi level, properties like the size of the nontrivial band gap, Fermi surface morphology, and flatness of the bands around valley K and K' can be further tuned via external stimuli such as an electric field or applying the biaxial strain. Our study gathers multiple degrees of freedom on a single platform and discusses their mutual interplay that could establish an excellent venue based on topological spintronics and valleytronics applications.

ACKNOWLEDGMENTS

This work was financially supported by the Natural Science Foundation of China (Grants No. 12034014 and No. 11974327), Fundamental Research Funds for the Central Universities (Grants No. WK3510000010 and No. WK2030020032), and Anhui Initiative in Quantum Information Technologies. The supercomputing services of AM-HPC and USTC are gratefully acknowledged.

-
- [1] O. Gunawan, Y. P. Shkolnikov, K. Vakili, T. Gokmen, E. P. De Poortere, and M. Shayegan, *Phys. Rev. Lett.* **97**, 186404 (2006).
- [2] J. R. Schaibley, H. Yu, G. Clark, P. Rivera, J. S. Ross, K. L. Seyler, W. Yao, and X. Xu, *Nat. Rev. Mater.* **1**, 16055 (2016).
- [3] X. Xu, W. Yao, D. Xiao, and T. F. Heinz, *Nat. Phys.* **10**, 343 (2014).
- [4] D. Xiao, G.-B. Liu, W. Feng, X. Xu, and W. Yao, *Phys. Rev. Lett.* **108**, 196802 (2012).
- [5] A. Rycerz, J. Tworzydło, and C. W. J. Beenakker, *Nat. Phys.* **3**, 172 (2007).
- [6] S. A. Vitale, D. Nezich, J. O. Varghese, P. Kim, S. A. Vitale, D. Nezich, J. O. Varghese, P. Kim, N. Gedik, P. J.-Herrero, D. Xiao, and M. Rothschild, *Small* **14**, 1801483 (2018).
- [7] D. Xiao, W. Yao, and Q. Niu, *Phys. Rev. Lett.* **99**, 236809 (2007).
- [8] W. Yao, S. A. Yang, and Q. Niu, *Phys. Rev. Lett.* **102**, 096801 (2009).
- [9] Majeed Ur Rehman and Z. A. Qiao, *Eur. Phys. J. B* **91**, 42 (2018).
- [10] Majeed Ur Rehman and A. A. Abid, *Chin. Phys. B* **26**, 127304 (2017).
- [11] D. Pesin and A. H. MacDonald, *Nat. Mater.* **11**, 409 (2012).
- [12] P. San-Jose, E. Prada, E. McCann, and H. Schomerus, *Phys. Rev. Lett.* **102**, 247204 (2009).
- [13] Y. S. Ang, S. A. Yang, C. Zhang, Z. Ma, and L. K. Ang, *Phys. Rev. B* **96**, 245410 (2017).
- [14] J. Li, R.-X. Zhang, Z. Yin, J. Zhang, K. Watanabe, T. Taniguchi, C. Liu, and J. Zhu, *Science* **362**, 1149 (2018).
- [15] I. Cucchi, A. Marrazzo, E. Cappelli, S. Ricco, F. Y. Bruno, S. Lisi, M. Hoesch, T. K. Kim, C. Cacho, C. Besnard, E. Giannini, N. Marzari, M. Gibertini, F. Baumberger, and A. Tamai, *Phys. Rev. Lett.* **124**, 106402 (2020).
- [16] K. Kandrai, P. Vancso, G. Kukucska, J. Koltai, G. Baranka, A. Hoffmann, A. Pekker, K. Kamaras, Z. E. Horvath, A.

- Vymazalova, L. Tapasztó, and P. N. Incze, *Nano Lett.* **20**, 5207 (2020).
- [17] A. Marrazzo, M. Gibertini, D. Campi, N. Mounet, and N. Marzari, *Nano Lett.* **19**, 8431 (2019).
- [18] R. Longuihos, A. Vymazalova, A. R. Cabral, and J. R.-Soares, *J. Phys.: Condens. Matter* **33**, 065401 (2021).
- [19] J. Zhang, B. Zhao, T. Zhou, Y. Xue, C. Ma, and Z. Yang, *Phys. Rev. B* **97**, 085401 (2018).
- [20] M. U. Farooq and J. Hong, *npj 2D Mater. Appl.* **3**, 3 (2019).
- [21] J. Zhang, B. Zhao, Y. Yao, and Z. Yang, *Phys. Rev. B* **92**, 165418 (2015).
- [22] Majeed Ur Rehman, X. Dong, T. Hou, Z. Li, S. Qi, and Z. Qiao, *Phys. Rev. B* **100**, 195422 (2019).
- [23] Y. Hou, J. Kim, and R. Wu, *Sci. Adv.* **5**, eaaw1874 (2019).
- [24] K. L. Seyler, D. Zhong, B. Huang, X. Linpeng, N. P. Wilson, T. Taniguchi, K. Watanabe, W. Yao, D. Xiao, M. A. McGuire, K.-M. C. Fu, and X. Xu, *Nano Lett.* **18**, 3823 (2018).
- [25] T. Norden, C. Zhao, P. Zhang, R. Sabirianov, A. Petrou, and H. Zeng, *Nat. Commun.* **10**, 4163 (2019).
- [26] Z. Zhang, X. Ni, H. Huang, L. Hu, and F. Liu, *Phys. Rev. B* **99**, 115441 (2019).
- [27] B. Zhai, J. Du, C. Shen, T. Wang, Y. Peng, Q. Zhang, and C. Xia, *Phys. Rev. B* **100**, 195307 (2019).
- [28] C. Ke, Y. Wu, W. Yang, Z. Wu, C. Zhang, X. Li, and J. Kang, *Phys. Rev. B* **100**, 195435 (2019).
- [29] L. Xu, M. Yang, L. Shen, J. Zhou, T. Zhu, and Y. P. Feng, *Phys. Rev. B* **97**, 041405(R) (2018).
- [30] J. Zhou, Q. Sun, and P. Jena, *Phys. Rev. Lett.* **119**, 046403 (2017).
- [31] Z. Liu, Y. Han, Y. Ren, Q. Niu, and Z. Qiao, *Phys. Rev. B* **104**, L121403 (2021).
- [32] P. E. Blöchl, *Phys. Rev. B* **50**, 17953 (1994).
- [33] G. Kresse and J. Furthmüller, *Phys. Rev. B* **54**, 11169 (1996).
- [34] J. P. Perdew, J. A. Chevary, S. H. Vosko, K. A. Jackson, M. R. Pederson, D. J. Singh, and C. Fiolhais, *Phys. Rev. B* **46**, 6671 (1992).
- [35] A. I. Liechtenstein, V. I. Anisimov, and J. Zaanen, *Phys. Rev. B* **52**, R5467 (1995).
- [36] S. Grimme, J. Antony, S. Ehrlich, and S. Krieg, *J. Chem. Phys.* **132**, 154104 (2010).
- [37] A. A. Mostofi, J. R. Yates, Y. S. Lee, I. Souza, D. Vanderbilt, and N. Marzari, *Comput. Phys. Commun.* **178**, 685 (2008).
- [38] G. Pizzi, V. Vitale, R. Arita, S. Blugel, F. Freimuth, G. Geranton, M. Gibertini, D. Gresch, C. Johnson, T. Koretsune *et al.*, *J. Phys.: Condens. Matter* **32**, 165902 (2020).
- [39] Q. Wu, S. Zhang, H.-F. Song, M. Troyer, and A. A. Soluyanov, *Comput. Phys. Commun.* **224**, 405 (2018).
- [40] See Supplemental Material at <http://link.aps.org/supplemental/10.1103/PhysRevB.105.165417> for simulation modeling details, interfacial characteristics, stability, orbital magnetization, Curie temperature estimation, and explanation associated with the switching of magnetic anisotropy energy, which includes Refs. [50–58].
- [41] D. Xiao, M.-C. Chang, and Q. Niu, *Rev. Mod. Phys.* **82**, 1959 (2010).
- [42] W. Feng, G.-Y. Guo, J. Zhou, Y. Yao, and Q. Niu, *Phys. Rev. B* **92**, 144426 (2015).
- [43] H. Zhou, C. Xiao, and Q. Niu, *Phys. Rev. B* **100**, 041406(R) (2019).
- [44] Q. Sun and N. Kioussis, *Phys. Rev. B* **97**, 094408 (2018).
- [45] J. Mao, S. P. Milovanovic, M. Andelkovic, X. Lai, Y. Cao, K. Watanabe, T. Taniguchi, L. Covaci, F. M. Peeters, A. K. Geim, Y. Jiang, and E. Y. Andre, *Nature (London)* **584**, 215 (2020).
- [46] S. Lisi, X. Lu, T. Benschop, T. A. d. Jong, P. Stepanov, J. R. Duran, F. Margot, I. Cucchi, E. Cappelli, A. Hunter *et al.*, *Nat. Phys.* **17**, 189 (2021).
- [47] Y. Fang, S. Wu, Z.-Z. Zhu, and G.-Y. Guo, *Phys. Rev. B* **98**, 125416 (2018).
- [48] D.-H. Kim, K. Kim, K.-T. Ko, J. H. Seo, J. S. Kim, T.-H. Jang, Y. Kim, J.-Y. Kim, S.-W. Cheong, and J.-H. Park, *Phys. Rev. Lett.* **122**, 207201 (2019).
- [49] C. Gong, L. Li, Z. Li, H. Ji, A. Stern, Y. Xia, T. Cao, W. Bao, C. Wang, Y. Wang, Z. Q. Qiu, R. J. Cava, Steven G. Louie, Jing Xia, and Xiang Zhang, *Nature (London)* **546**, 265 (2017).
- [50] X. Li, M.-W. Lin, J. Lin, B. Huang, A. A. Puretzky, C. Ma, K. Wang, W. Zhou, S. T. Pantelides, M. Chi, I. Kravchenko, J. Fowlkes, C. M. Rouleau, D. B. Geohegan, and K. Xiao, *Sci. Adv.* **2**, e1501882 (2016).
- [51] Y. Shi, W. Zhou, A.-Y. Lu, W. Fang, Y.-H. Lee, A. L. Hsu, S. M. Kim, K. K. Kim, H. Y. Yang, L.-J. Li, J.-C. Idrobo, and J. Kong, *Nano Lett.* **12**, 2784 (2012).
- [52] M. Zhao, M. Liu, Y. Dong, C. Zou, K. Yang, Y. Yang, L. Zhang, and S. Huang, *J. Mater. Chem. C* **4**, 10215 (2016).
- [53] K. Zollner, M. Gmitra, and J. Fabian, *Phys. Rev. Lett.* **125**, 196402 (2020).
- [54] S. L. Dudarev, G. A. Botton, S. Y. Savrasov, C. J. Humphreys, and A. P. Sutton, *Phys. Rev. B* **57**, 1505 (1998).
- [55] S. Grimme, *J. Comput. Chem.* **27**, 1787 (2006).
- [56] D.-S. Wang, R. Wu, and A. J. Freeman, *Phys. Rev. B* **47**, 14932 (1993).
- [57] C. Gong, Eun M. Kim, Y. Wang, G. Lee, and X. Zhang, *Nat. Commun.* **10**, 2657 (2019).
- [58] X. Sui, T. Hu, J. Wang, B.-L. Gu, W. Duan, and M.-S. Miao, *Phys. Rev. B* **96**, 041410(R) (2017).